

# Seeing the forest for the trees: hierarchical generative models for star clusters from hydro-dynamical simulations

Stefano Torniamenti,<sup>1,2,3</sup>★ Mario Pasquato,<sup>2,4</sup> Pierfrancesco Di Cintio,<sup>5,6,7</sup>  
Alessandro Ballone,<sup>1,2,3</sup> Giuliano Iorio,<sup>1,2</sup> Michela Mapelli<sup>1,2,3</sup>

<sup>1</sup> *Physics and Astronomy Department Galileo Galilei, University of Padova, Vicolo dell'Osservatorio 3, I-35122, Padova, Italy*

<sup>2</sup> *INFN- Sezione di Padova, Via Marzolo 8, I-35131 Padova, Italy*

<sup>3</sup> *INAF, Osservatorio Astronomico di Padova, vicolo dell'Osservatorio 5, 35122 Padova, Italy*

<sup>4</sup> *Center for Astro, Particle and Planetary Physics (CAP<sup>3</sup>), New York University Abu Dhabi*

<sup>5</sup> *Physics and Astronomy Department, University of Firenze, via G. Sansone 1, I-50019 Sesto Fiorentino, Italy*

<sup>6</sup> *INFN - Sezione di Firenze, via G. Sansone 1, I-50019 Sesto Fiorentino, Italy*

<sup>7</sup> *CREF, Via Panisperna 89A, I-00184 Rome, Italy*

Accepted XXX. Received YYY; in original form ZZZ

## ABSTRACT

Star formation in molecular clouds is clumpy, hierarchically subclustered. Fractal structure also emerges in hydro-dynamical simulations of star-forming clouds. Simulating the formation of realistic star clusters with hydro-dynamical simulations is a computational challenge, considering that only the statistically averaged results of large batches of simulations are reliable, due to the chaotic nature of the gravitational  $N$ -body problem. While large sets of initial conditions for  $N$ -body runs can be produced by hydro-dynamical simulations of star formation, this is prohibitively expensive in terms of computational time. Here we address this issue by introducing a new technique for generating many sets of new initial conditions from a given set of star masses, positions and velocities from a hydro-dynamical simulation. We use hierarchical clustering in phase space to learn a tree representation of the spatial and kinematic relations between stars. This constitutes the basis for the random generation of new sets of stars which share the clustering structure of the original ones but have individually different masses, positions, and velocities. We apply this method to the output of a number of hydro-dynamical star-formation simulations, comparing the generated initial conditions to the original ones through a series of quantitative tests, including comparing mass and velocity distributions and fractal dimension. Finally, we evolve both the original and the generated star clusters using a direct  $N$ -body code, obtaining a qualitatively similar evolution.

**Key words:** ISM: kinematics and dynamics – open clusters and associations: general – ISM: clouds – methods: numerical – methods: statistical

## 1 INTRODUCTION

A large fraction of star formation happens in clusters (Lada & Lada 2003; but see also the recent findings by Reina-Campos et al. 2019 and Ward et al. 2020). The formation and early evolution of star clusters is currently not fully constrained. Several open issues are related to this, such as the puzzle of the origin and nature of multiple populations in globular clusters (e.g., Lee et al. 1999; D'Antona & Caloi 2004; Gratton et al. 2004; D'Antona & Ventura 2007; Decressin et al. 2007; Marino et al. 2008; D'Ercole et al. 2008; Milone et al. 2009; Ventura & D'Antona 2009; Carretta et al. 2009; D'Ercole et al. 2010; Gratton et al. 2012; Krause et al. 2013; Bastian & Lardo 2015; Piotto et al. 2015; D'Antona et al. 2016; Bastian &

Lardo 2018; Gratton et al. 2019) and the related horizontal-branch morphology ‘second parameter’ problem (e.g., Lee et al. 1994; D'Antona et al. 2002; Lee et al. 2005; Pasquato et al. 2013, 2014; Tailo et al. 2015, 2020). Other, more loosely related issues are the question whether observed scaling laws for these systems are primordial or dynamical, locally set or universal (e.g., Djorgovski 1995; Pasquato & Bertin 2008, 2010; Zaritsky et al. 2011; Pang et al. 2018), the contribution of star clusters to the Galactic halo and their complex co-evolution with the disk (e.g., Cantat-Gaudin 2015; Antoja et al. 2018; Gaia Collaboration et al. 2018; Chung et al. 2019; Cantat-Gaudin et al. 2020; Pasquato & Masiuk 2019; Dinnbier & Kroupa 2020; Pang et al. 2020), the retention/ejection mechanism for dark remnants (e.g., Kulkarni et al. 1993; Drukier 1996; Davies & Hansen 1998; Baumgardt et al. 2004; Banerjee et al. 2010; Breen & Heggie 2013; Alessandrini et al. 2016), and

★ E-mail: stefano.torniamenti@studenti.unipd.it

the mechanism of formation of intermediate-mass black holes (e.g., Bahcall & Ostriker 1975; Portegies Zwart et al. 2004; Baumgardt et al. 2005; Pasquato et al. 2009; Safonova & Shastri 2010; Beccari et al. 2010; Vesperini et al. 2010; Umbreit & Rasio 2013; Leigh et al. 2014; Mapelli 2016; Pasquato et al. 2016; de Vita et al. 2017).

Gravitational  $N$ -body simulations are a key tool to model star cluster evolution, but they often start from rather idealized initial conditions, often sampled from equilibrium models, such as the Plummer (1911) sphere. Even though more sophisticated models are available (e.g., Lynden-Bell 1962; Michie & Bodenheimer 1963; King 1966; Prendergast & Tomer 1970; Wilson 1975; Bertin & Stiavelli 1984; Lupton & Gunn 1987; Trenti & Bertin 2005; An & Evans 2006; Varri & Bertin 2012; Gieles & Zocchi 2015; Daniel et al. 2017; Claydon et al. 2019), these were developed with the goal of describing the current, quasi-equilibrium state of star clusters. Thus, by design, they bear little resemblance to observed primordial conditions in embedded clusters, which are clumpy, hierarchical and possibly far from virial equilibrium (e.g., Lada & Lada 2003; Bastian et al. 2009; Dib & Henning 2019). For more than a decade, fractal initial conditions have been used as a starting point for realistic simulations (e.g., Goodwin & Whitworth 2004; Allison et al. 2010; Kuepper et al. 2011; Küpper et al. 2011; Parker et al. 2011, 2014; Park et al. 2018; Di Carlo et al. 2019), but even this approach does not guarantee that all the relevant characteristics of the actual primordial conditions of star clusters are correctly captured.

For instance, clumpiness in embedded star clusters is not the only feature that sets realistic initial conditions apart from idealized models, as rotation also plays an important role. For example Corasaro et al. (2017) have shown that the rotation signature from the parent molecular cloud persists in the alignment of stellar spins in some open clusters, even today. Such result has been theoretically supported also by Lee & Hennebelle (2016), Mapelli (2017), and Ballone et al. (2020). Globular clusters are also consistently found to rotate, sometimes with significant dynamical effects (Bianchini et al. 2013; Fabricius et al. 2014; Ferraro et al. 2018; Kamann et al. 2018; Dalessandro et al. 2021).

A seemingly obvious but computationally demanding way to generate realistic initial conditions for star clusters is to run suites of hydro-dynamical simulations, coupled with appropriate recipes for handling star formation and other sub-grid physics (e.g., Klessen & Burkert 2000; Bonnell et al. 2003; Bate 2009; Federrath & Klessen 2012; Krumholz et al. 2012; Dale et al. 2015; Fujii & Portegies Zwart 2016; Geen et al. 2016; Seifried et al. 2017; Zamora-Avilés et al. 2019; Lee & Hennebelle 2019; Wall et al. 2019). Despite these efforts, large sets of simulations including all the relevant physics are at present hard to come by, notwithstanding ever-advancing hardware capabilities. This is compounded by the fact that  $N$ -body simulations, even direct-summation ones, eventually diverge from the true solution of the  $N$ -body problem for most initial conditions due to numerical errors and the chaotic nature of the problem (e.g. see Goodman et al. 1993; Hensendörff & Merritt 2002; Kandrup & Sideris 2003; Boekholt & Portegies Zwart 2015; Di Cintio & Casetti 2019, 2020; Manwadkar et al. 2020; Wang & Hernandez 2021 and references therein), with the consequence that only ensemble-averaged results are considered reliable within the current consensus. To obtain such averages, multiple  $N$ -body runs are needed, each with its own initial conditions.

Here we introduce a new approach to generate new realizations from a given output of a hydro-dynamical simulation, at a tiny fraction of the computational cost of running an additional independent simulation. The generated realizations are qualitatively similar to

the original ones when observed in 3D space and pass a series of quantitative comparisons.

The paper is organized as follows. In Section 2, we recap the properties of the hydro-dynamical simulations we used to generate our original initial condition sets; Section 3 presents our approach for generating new realizations, while in Section 4 we describe our results and run various checks to compare the generated realizations to the original simulations. In Section 5, we discuss and draw conclusions.

## 2 SMOOTHED-PARTICLE HYDRO-DYNAMICAL SIMULATIONS

### 2.1 Initial conditions and simulation set-up

As a starting point for this work, we used the sink particles from 10 smoothed-particle hydrodynamics (hereafter SPH) simulations of molecular clouds performed by Ballone et al. (2020) using the GASOLINE2 code (Wadsley et al. 2004, 2017). In the following, we may refer to these sink particles as ‘stars’ for convenience.

The initial conditions of the SPH simulations are spherical molecular clouds with total gaseous mass in the range  $10^4 \leq M_{\text{mc}}/M_{\odot} \leq 10^5$  (see the last column of Table 1), uniform temperature  $T_0 = 10$  K and uniform density  $2.5 \times 10^2 \text{ cm}^{-3}$ . All runs have a fixed number of initial SPH particles equal to  $10^7$ , corresponding to a gas mass resolution of  $10^{-3}$  (for the least massive molecular cloud) to  $10^{-2} M_{\odot}$ . Stars form during the simulation by means of a sink particle algorithm based on the same prescriptions as Bate et al. (1995).

In order to induce a non-isotropic evolution, the SPH gas particles are initially given a turbulent, divergence-free, Gaussian random velocity field with a different random seed for each simulation of the set, following a Burgers (1948) power spectrum. The velocity power is set to have clouds in an initial marginally bound state so that their initial virial ratio  $\alpha_{\text{vir}} \equiv 2K/|W| = 2$ , where  $K$  and  $W$  are the gas kinetic and potential energy, respectively. During the hydro-dynamical simulation, the gas equation of state has been set to be adiabatic, but radiative cooling by dust has been modeled as in Boley (2009) and Boley et al. (2010). The amount of energy lost by cooling was calculated through the divergence of the heat flux

$$\nabla \cdot F_{\text{cool}} = - \frac{(36\pi)^{1/3} \sigma (T^4 - T_{\text{irr}}^4)}{s(\Delta\tau + 1/\Delta\tau)}. \quad (1)$$

In the Equation above,  $\sigma$  is the Stefan-Boltzmann constant,  $T$  the gas temperature,  $T_{\text{irr}}$  the irradiation temperature,  $s = (m/\rho)^{1/3}$  and  $\Delta\tau = s k \rho$ , where  $m$  and  $\rho$  are the gas particle mass and density and  $k$  is the local opacity. For  $k$ , the adopted Planck and Rosseland dust opacities are taken from D’Alessio et al. (2001), while  $T_{\text{irr}}$  was set to 10 K.

No stellar feedback was included in this set of simulations and we simply decided to assume that our clusters are the result of instantaneous gas removal at 3 Myr after the beginning of the hydro-dynamical simulation, to roughly simulate the effect of the first supernova explosion. Dale et al. (2015) have shown that the pre-supernova gas removal is expected to play a minor effect on the survival and dynamics of stellar clusters and indeed we also checked that at 3 Myr the gas accounts for a small fraction of the mass where most of the stellar mass is residing. Furthermore, at 3 Myr all the clouds converted about 30–40% of their gas mass into sink particles, in agreement with previous hydro-dynamical simulations showing that stellar feedback should lead to a maximum star

**Table 1.** Properties of the end states of the SPH simulations of Ballone et al. (2020).

Name	$N_s$	$N_c$	$\alpha_{\text{vir}}$	$\gamma$	$M_{\text{sink}} [\text{M}_\odot]$	$M_{\text{mc}} [\text{M}_\odot]$
m1e4	2523	6	1.19	2.30	$4.22 \times 10^3$	$10^4$
m2e4	2571	4	1.32	2.12	$6.69 \times 10^3$	$2 \times 10^4$
m3e4	2825	5	1.48	2.20	$1.03 \times 10^4$	$3 \times 10^4$
m4e4	2868	2	1.47	2.17	$1.44 \times 10^4$	$4 \times 10^4$
m5e4	2231	4	1.47	1.80	$1.41 \times 10^4$	$5 \times 10^4$
m6e4	3054	5	1.69	2.15	$2.04 \times 10^4$	$6 \times 10^4$
m7e4	4214	9	1.50	2.20	$3.15 \times 10^4$	$7 \times 10^4$
m8e4	2945	6	1.60	1.86	$2.83 \times 10^4$	$8 \times 10^4$
m9e4	3161	4	1.52	1.90	$3.05 \times 10^4$	$9 \times 10^4$
m1e5	3944	6	1.46	2.20	$3.80 \times 10^4$	$10^5$

After the name of each simulation (Col. 1) we report the number of stars generated (Col. 2), the number of macroscopic subclumps (Col. 3), the virial ratio ( $\alpha_{\text{vir}} \equiv 2K/|W|$ , Col. 4), the  $\gamma$  coefficient of the mass-spectrum fitting function of eq. 2 (Col. 5), the total mass of the stars (Col. 6), and the mass of the parent molecular cloud (Col. 7).

formation efficiency of about this amount (e.g., Vázquez-Semadeni et al. 2010; Dale et al. 2015; Gavagnin et al. 2017; Li et al. 2019). For more details on such choices, we refer the reader to Ballone et al. (2020).

## 2.2 Structural properties of the SPH simulations

Independently of the specific initial value of  $M_{\text{mc}}$ , our SPH simulations present a clumpy structure with  $N_s \approx 3 \times 10^3$  stars organized in a maximum of  $N_c = 9$  main subclumps for m7e4 to a minimum of 2 for m4e4<sup>1</sup>. Figure 1 shows the  $x-y$ ,  $y-z$  and  $z-x$  projections of the stars position on the three coordinate planes for the system m1e4, with their masses  $m$  shown in colour. We find a rather prominent primordial mass segregation, with heavier stars typically found within the central regions of the main clumps and lighter stars at large distance from the geometric centres of such subsystems. All systems are above the virial condition, with  $\alpha_{\text{vir}}$  ranging from 1.19 for the m1e4 case, to 1.69 for m6e4.

In order to quantify the properties of the end states of the SPH simulations, we have also evaluated their distributions of inter-particle distances, mass spectrum and velocity  $f(d)$ ,  $f(m)$  and  $f(v)$ . Figure 2 shows these distributions for the sink particles of the simulations m1e4, m3e4, m5e4, m7e4 and m9e4. The distribution of inter-particle distances  $d$  shows a quite complex structure with several slope changes. The clumpy structure of the particles' spatial distribution gives rise to several peaks in  $f(d)$ , corresponding to the distances between clumps themselves. This can be observed clearly in the left panel of Fig. 2. For the specific case of the m1e4, the peaks are located roughly at 0.1, 0.45, 1.75 and 3 pc (as highlighted by the vertical dotted lines), that can be easily identified as the distances between the approximate centres of the main clumps of particles shown in Fig. 1.

The mass spectra of the sink particles all approximately follow the same power-law structure between a low-mass and a high-mass cut-off. We have fitted the numerically recovered mass spectra with

the *bona-fide* function

$$f(m) = \frac{C}{(m^2 + m_*^2)^{\gamma/2}}, \quad (2)$$

where  $C$  is a normalization constant,  $m_*$  is a scale mass, that for the explored systems is always in the range between 0.8 and 4  $\text{M}_\odot$ , while exponent  $\gamma$  ranges from  $\approx 1.8$  to  $\approx 2.3$ .

The velocity distributions  $f(v)$  do not show a relevant dependence on the specific initial value of  $M_{\text{mc}}$ , as shown in the right hand panel of Fig. 2. Qualitatively, the velocity distribution is well described by a Maxwell-Boltzmann from  $v = 0$  to 5  $\text{km s}^{-1}$  (value corresponding to the peak of  $f(v)$ ) and then shows a  $v^{-3}$  power-law trend. The properties of the SPH simulations are summarized in Table 1.

## 3 METHODS

In the following, we describe our new procedure to build a generative model of star cluster initial conditions. In the context of supervised classification, where the goal is to predict a label  $Y$  given a set of features  $X$  (see, e.g., Chardin & Bianchini 2021), generative models are usually contrasted to discriminative models, with the former seeking to model the joint distribution  $p(X, Y)$  and the latter focusing on just the conditional probability distribution  $p(Y|X)$  (Jebara 2012). A model of the joint distribution is valuable even if we do not intend to perform classification, as in our case. More generally, a generative model's goal is to learn a representation of an intractable distribution given an usually finite number of samples. The generator typically maps from a latent domain on which a simple distribution is defined, such as a multivariate Gaussian on  $R^n$ , to the complex data domain (e.g. Ruthotto & Haber 2021). Recently, most of the interest in generative models is driven by deep learning approaches, such as generative adversarial networks (Goodfellow et al. 2014). However, in principle, much simpler models such as hidden Markov models (Rabiner & Juang 1986; Eddy 2004) or grammars (e.g., Chomsky 1959; Jelinek et al. 1992; Beaumont & Stepney 2009) meet the definition of a generative model in the broader sense defined above. The latter have proved useful in the description and generation of objects displaying fractal structure, as in the case of Lindenmayer systems applied to plant growth (Lindenmayer 1968a,b; Prusinkiewicz & Hanan 2013).

Our approach focuses on reproducing the multi-fractal structure of embedded star clusters generated by hydro-dynamical simulations by capturing the relations between subclusters at different scales in terms of a hierarchical clustering tree, allowing us to generate new realizations by modifying the first branches of the tree. These branches describe the macro structure, i.e. the relations between large subclusters. The parameters that characterize these first branches can then be treated as the latent domain of our generative model. In the following, we will make this intuition more precise by relying on a hierarchical clustering tree learned by an agglomerative clustering algorithm (see Kaufman & Rousseeuw 1990).

We proceed in two steps. First, we use a hierarchical clustering algorithm to identify clumps of stars in the phase space of the original hydro-dynamical simulation output. The clumps are organized by the algorithm into a tree  $\mathcal{T}$ , where the root node contains the whole set of stars and each subsequent node represents a two-way split with each branch being a clump of stars, down to the leaf nodes representing individual stars. To describe the relevant properties of the clumps, we assume that the phenomena leading to star formation

<sup>1</sup> Subclumps are identified heuristically as groups of neighbouring stars containing more than 0.05  $N_s$ , whose self potential energy exceeds that of the rest of the system.

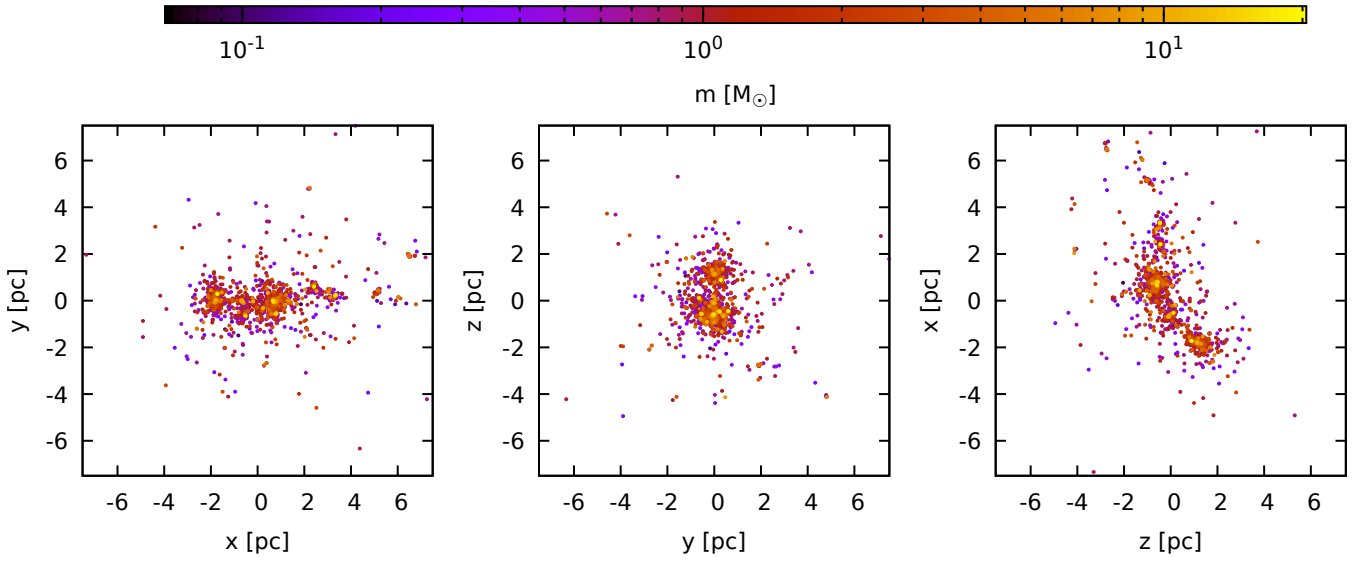


**Figure 1.** From left to right, projections in the  $x - y$ ,  $y - z$  and  $z - x$  planes of the end state of the **m1e4** simulation. The colour map marks the mass of the individual stars in units of  $M_{\odot}$ .

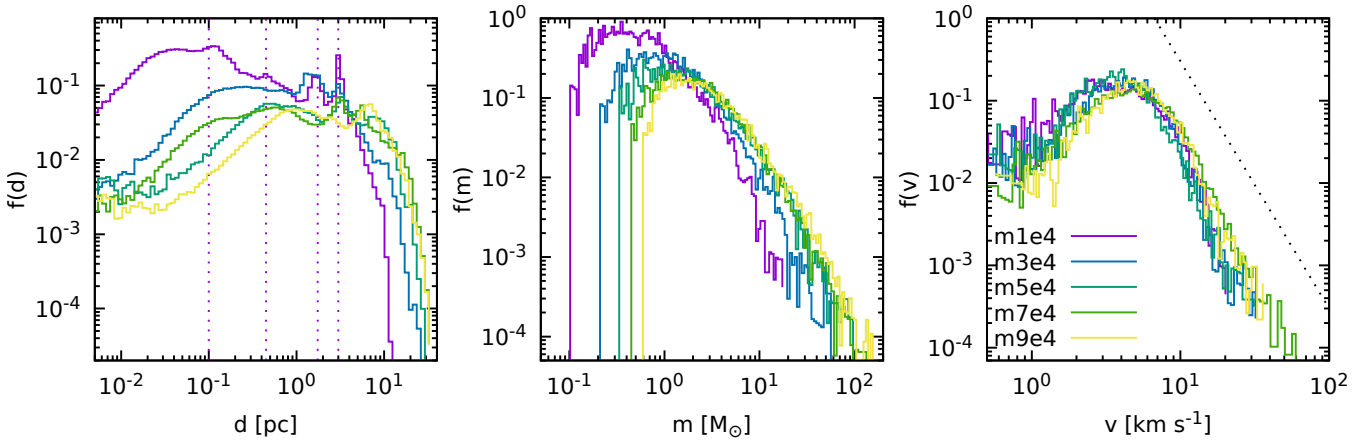


**Figure 2.** Distribution of inter-particle distances  $f(d)$  (left-hand panel, main), mass spectra  $f(m)$  (middle panel), and velocity distribution  $f(v)$  (right-hand panel) for the sink particles taken from the simulations **m1e4**, **m3e4**, **m5e4**, **m7e4**, **m9e4**. The vertical dotted lines in the left hand panel mark the position of the main peaks of  $f(d)$  corresponding to the distances between the main subclusters for the **m1e4** case, while the thin dotted line in the right-hand panel mark the  $v^{-3}$  power-law trend of the velocity distributions.

are rotation invariant. Note that this does not mean that any specific realization of stellar positions and velocities must be isotropic, but that all orientations of (possibly anisotropic) realizations are equally likely. This is warranted at least in hydro-dynamical simulations, where initial conditions are approximately isotropic. With the assumption of rotation invariance, we can concentrate on just the modulus of the distance  $\delta = |\delta|$  between the centres of mass of the clumps (dropping the information regarding the absolute orientation of the distance vector), the modulus of their relative velocity  $u = |\mathbf{u}|$ , the angle between the position and relative velocity vector  $\theta = \arccos(\delta \cdot \mathbf{u} (\delta u)^{-1})$ , and the mass ratio between two clumps. To describe how the mass is split at each node we refer to  $r_m$ , defined as the ratio between the lightest of the two resulting groups and the total mass of the node. With this definition, mass ratios fall between 0 (maximally unequal split) and 0.5 (equal-mass split).

Second, we generate a new realization of particle positions and

velocities by placing clumps of stars (and sub-clumps down to the individual stars) in phase space. To build a new realization of total mass  $M$  (details in Sect. 3.3), we start with one particle at rest in the origin of our coordinate system, initially containing the total mass of the cluster  $M$ . Then we iteratively split it into new particles and place them at a distance  $\delta_i$  from each other, moving with relative velocity  $\mathbf{u}_i$ . The relevant variables  $\delta_i$ ,  $\mathbf{u}_i$ ,  $\theta_i$ , and the relevant mass ratio  $r_i$  are taken from the tree  $\mathcal{T}$  at each iteration step  $i$  except for the first step(s), which are drawn from a tree  $\mathcal{T}'$  built on a different simulation. While this does not guarantee that the outcome will be described by a tree with statistical properties that match those of  $\mathcal{T}$ , it is at least heuristically convincing in the case of very hierarchical distributions. Moreover, we will check ex post that the realizations generated in this way have a set of desirable properties with respect to the original cluster.

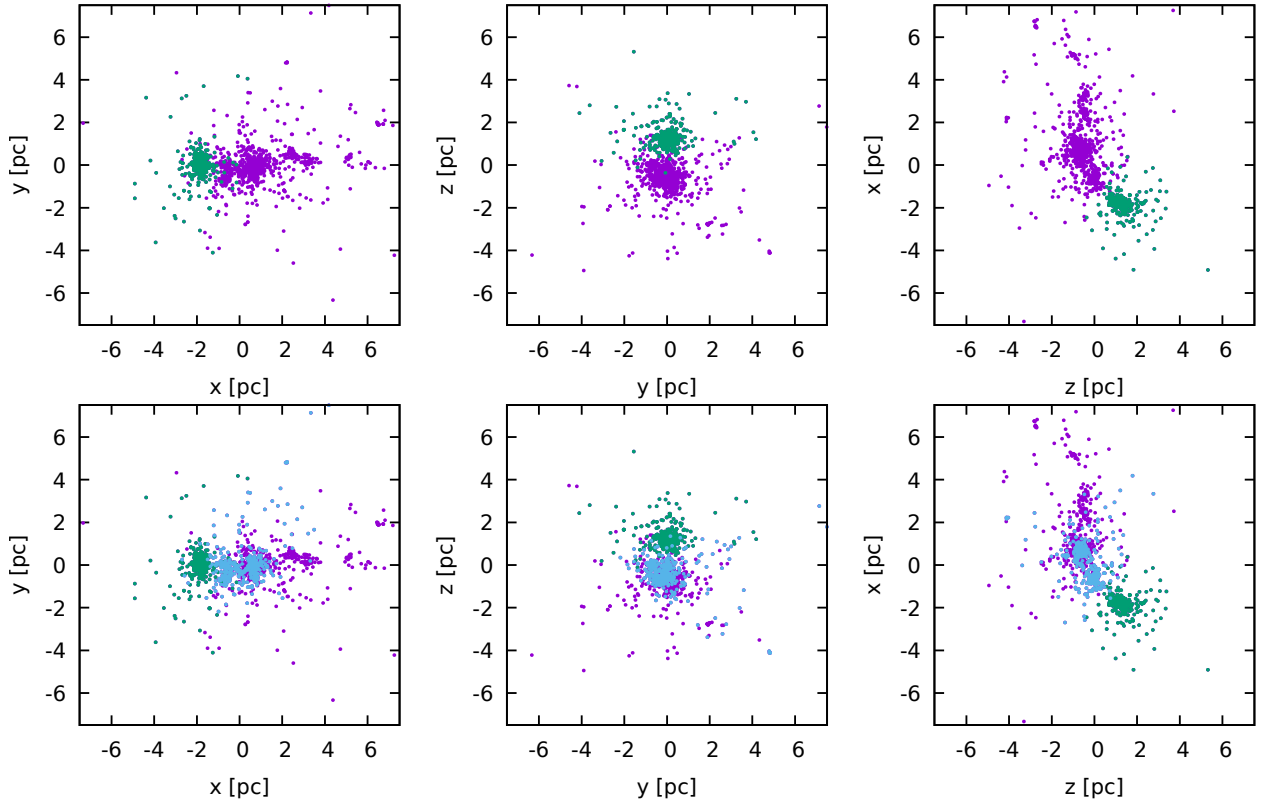


**Figure 3.** The first node from the trunk in the *AGNES* tree splits the sink particles of the *m1e4* simulation in two groups (green and purple in the upper panel row). With the second node the purple group is split further in two subgroups (purple and cyan, lower panel row).

### 3.1 Hierarchical clustering

Hierarchical clustering algorithms arrange data into a tree-like structure representing nested groups, capturing clustering structure at different scales. In particular, we use an agglomerative clustering algorithm (see the chapter on *AGNES* in [Kaufman & Rousseeuw 1990](#)). This means that the tree-like hierarchy of clusters is built from the bottom up: the algorithm starts from individual points, and then merges the most similar ones into clusters until some stopping criterion is satisfied (e.g., until only a specified number of clusters are left). This way of proceeding can be thought as drawing a tree with a branch for every pair of clusters that merge. A dendrogram can be used to display the resulting tree structure, with leaf nodes corresponding to individual points and the root corresponding to the whole data set. We refer the interested reader to [Pasquato & Milone \(2019\)](#) for an illustration of this and other clustering algorithms in an astronomical context. Here, we selected this algorithm because it is well suited for studying the complex structure of the hydro-dynamical simulations described in Section 2, since it is informative on very different scales and it can capture clusters (and sub-clusters) of various sizes. We use the implementation offered by the *SCIKIT-LEARN* library ([Pedregosa et al. 2011](#)).

#### 3.1.1 Linkage

Moving towards the root of the tree, an agglomerative clustering algorithm merges at each node either two groups with each other or a lone point into a group. This is based on a notion of (dis)similarity between groups which may be defined in multiple ways, or linkages.

A linkage is a prescription for defining the dissimilarity between groups in the context of hierarchical clustering. A simple example is the so-called single linkage approach, where the distance between two groups is defined to be equal to the minimum distance between any points in the two groups<sup>2</sup> as  $\Delta_{AB} := \min(\delta_{i \in A, j \in B})$ , where  $i$  and  $j$  represent sink particles belonging to group  $A$  and  $B$ , respectively, and  $\delta_{ij}$  is the distance between two such particles. However, in our context this prescription would result in elongated groups of sinks, as two blobs that just touch in one point get merged into one pretty quickly, even if their centres-of-mass are far from each other. A visual inspection of the sink particle distribution reveals rounder clumps than we would obtain this way, as shown, e.g., in Fig. 3. Thus we used the [Ward \(1963\)](#) linkage prescription instead of single linkage. Ward’s linkage is defined as follows:

$$\Delta_{AB}^2 = \sum_{i \in A \cup B} \delta_{ic_{A \cup B}}^2 - \left( \sum_{i \in A} \delta_{ic_A}^2 + \sum_{i \in B} \delta_{ic_B}^2 \right), \quad (3)$$

where the index  $i$  denotes the generic  $i$ -th particle and  $c_A$ ,  $c_B$ , and  $c_{A \cup B}$  denote the centroids of sets  $A$ ,  $B$ , and  $A \cup B$  respectively. Equation 3 corresponds to the increase in variance with respect to the relevant centroids as groups  $A$  and  $B$  are merged. Merging groups decreases the number of centroids by one, so variance is bound to

<sup>2</sup> Such scheme is commonly dubbed as friend-of-friends prescription in the context of halo-finding in cosmological simulations ([Davis et al. 1985](#)) or galaxy clusters from observational data ([Murphy et al. 2012](#)). See also [Feng & Modi \(2017\)](#) and references therein.



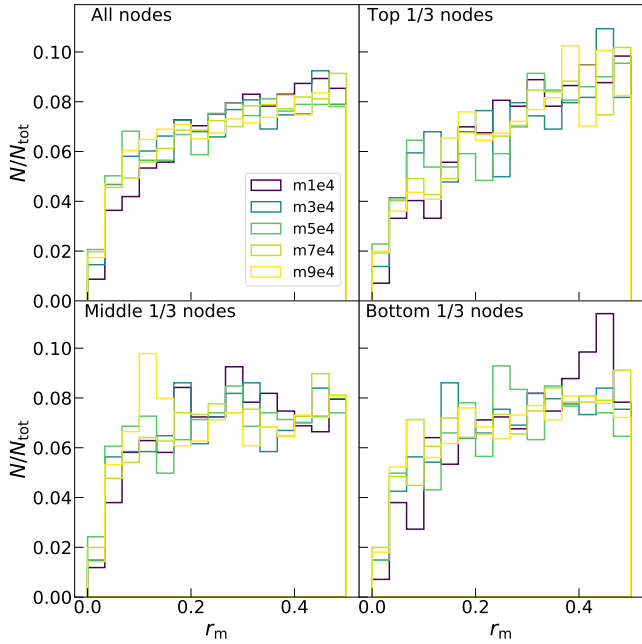


**Figure 4.** Distribution of the mass of the lightest of the two resulting groups at any given split, in units of the parent group. The top left panel shows the histogram of mass ratios calculated for all nodes in the learned tree. The top right panel shows the mass ratios for the top 1/3 of the nodes from the root (big clumps), the bottom left for the middle 1/3 (intermediate-size clumps), and the bottom right for the lower 1/3 (small clumps to individual stars).

increase, but using Ward’s linkage results in cluster mergers that minimize its increase at each step.

### 3.2 Application of hierarchical clustering to stellar clusters

We applied agglomerative clustering to the stellar clusters from hydro-dynamical simulations introduced in Section 2. The tree is built relying on euclidean distance between sink particles in the phase space as a measure of dissimilarity, so that particles sharing both similar positions and similar velocities tend to be grouped together. Before applying the algorithm, we scaled the positions and the velocities by their standard deviations. This step or some such is necessary so that the result of our clustering does not depend on the arbitrary choice of the unit of measurement of time.

Figure 3 shows the groups of sink particles corresponding to the first two nodes of the learned tree (starting from the root). The first node splits the sinks into two big chunks, and the second node splits off a smaller clump from one of these<sup>3</sup>. Our choice of using Ward linkage results in the splitting off of the most massive sub-clumps in the first branches of the tree, leading to an overall balanced tree. The first splitting thus gives information about the distribution of the sub-clumps at large scales and, moving towards the leaves of the trees, sub-clusters are split in smaller and smaller sub-clumps, as desired for our task.

Figure 4 shows the mass ratios between sub-clumps branching off at different depths within the tree. The distribution of mass ratios is not particularly affected by tree depth. This is expected if

<sup>3</sup> Even as we describe the tree from the root up (writing occasionally in terms of splits/splitting) agglomerative methods build the tree from the leaves, i.e. the individual sink particles.

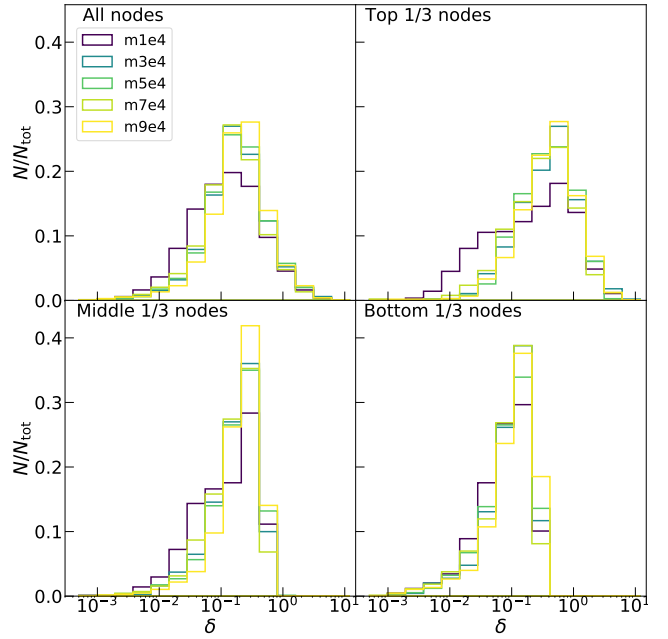


**Figure 5.** Same as Figure 4 but for the distribution of the distances (scaled by their variance) between the centres-of-mass of two different branches of the AGNES tree.

the structure of the sink particle distribution is scale invariant, as moving down the tree (towards the leaves) probes smaller scales by construction. Additionally, Fig. 4 shows that the distribution is similar across different simulations, spanning a range of total mass of an order of magnitude. To assess if the mass-ratios can be considered as drawn from the same distribution (after properly rescaling the mass), we performed pairwise Kolmogorov–Smirnov tests. Despite multiple testing we never obtain a p-value below  $10^{-2}$ , so we have no reason to suspect that the distributions are different.

Similar information on the scaling behavior of our simulations can be extracted from Figures 5 and 6, where we show the distribution of the distances between the clumps and that of their relative velocities. In particular, the positions of the maximums of the distributions shift towards lower values by moving from the top to the bottom nodes, confirming that the tree is considering smaller and smaller scales. Also in this case, all the simulations show very similar distributions at each level for both the distances and the relative velocities. The distribution of the angles between the relative velocity and the distance is shown in Figure 7. This distribution appears flat except for a rise at  $\cos \theta \approx 1$  which corresponds to relative velocity parallel to the separation vector between clumps, which is expected in a super-virial cluster undergoing overall expansion.

Relevant physical information can be drawn by considering the relation between quantities of the same node in the AGNES tree. Figure 8 shows the relation between the distance of the sub-clumps and their relative velocity, for each node. The main sub-clumps, that correspond to the nodes closest to the root, show a direct proportionality between these two quantities, possibly due to rigid rotation. In contrast, on the smallest scales, the single particle relative velocity shows a tendency to decline with the square root of their distance, as would happen for two clumps (or even two individual stars) orbiting one another under the influence of each other’s monopole potential. Interestingly, all relative motions between clumps take place between the rigid and Keplerian extremes.

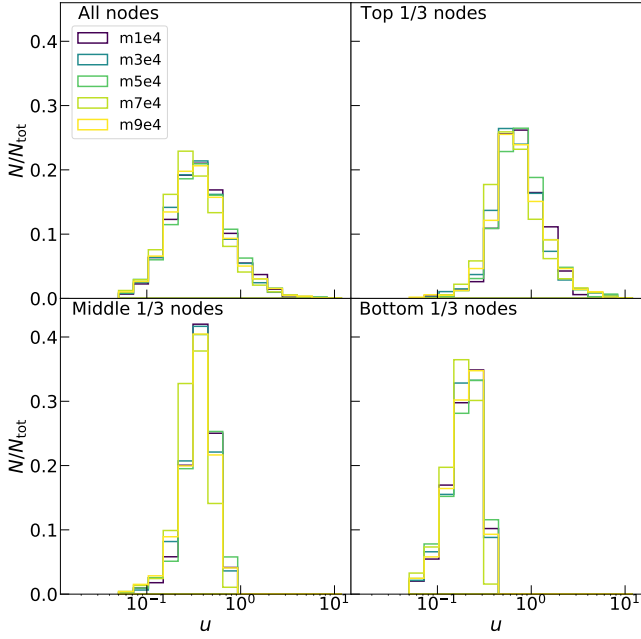


**Figure 6.** Same as Figure 4 but for the distribution of the relative velocities (scaled by their variance) between the centres-of-mass of two different branches of the AGNES tree.

### 3.3 Generating new realizations

As explained in Section 3.2, the application of the agglomerative clustering algorithm to stellar clusters allows us to learn a tree  $\mathcal{T}$  encoding their hierarchical structure. Each node of the tree  $\mathcal{T}_i$  is associated to the relevant properties ( $\delta_i$ ,  $\mathbf{u}_i$ ,  $\theta_i$ , and  $r_i$ ) quantifying the relations between the sub-clumps corresponding to the branches departing from the node. Thus the tree essentially encodes instructions to generate a new star cluster, as it can be traversed from the top, iteratively splitting an initial particle until the leaf level is reached, where individual stars have been produced. In our case, the goal is to change the cluster at the global structure level -nearest to the trunk of the tree-, thus creating different sub-clumps configurations while preserving the small scale properties of the sub-clumps (such as their fractal structure). We thus take the quantities  $\delta_i$ ,  $\mathbf{u}_i$ ,  $\theta_i$ , and  $r_i$  associated to the nodes  $\mathcal{T}_i$  for  $i < k$  and replace them with the quantities  $\delta'_i$ ,  $\mathbf{u}'_i$ ,  $\theta'_i$ , and  $r'_i$  associated to the nodes  $\mathcal{T}'_i$  of another tree  $\mathcal{T}'$ , learned from a different set of sink particles. This grafting procedure represents a way to combine the large scale properties of one simulation with the small scale properties of another. For the results presented in Sect. 4, these nodes are sampled randomly from other simulations.

The generation procedure is implemented as follows. First, we consider a particle with a mass  $M_1$  equal to the total mass of the cluster considered, placed at the centre of mass of the cluster. The particle is first split into two particles of masses  $M_{11}$  and  $M_{12}$  such that  $M_{11} + M_{12} = M_1$  and  $\min(M_{11}, M_{12})/M_1 = r'_1$ . The positions and velocities of the new particles are assigned such that their centre of mass is at rest in the origin of the system, their distance vector is  $\delta'_1$ , and their relative velocity  $\mathbf{u}'_1$ , with an angle  $\theta'_1 = \arccos(\delta'_1 \cdot \mathbf{u}'_1 / (\delta'_1 u'_1))$ . This splitting procedure is then repeated until a cluster with the same number of particles as the reference one is obtained. At each step, the particle-to-split is chosen by considering the same order of splitting as the original

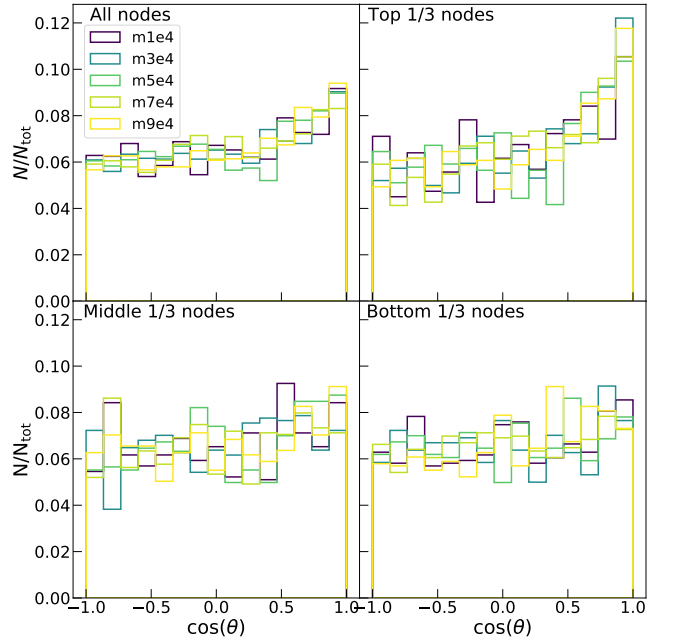


**Figure 7.** Same as Figure 4 but for the distribution of the cosine of the angle between relative velocity and distance of the centres-of-mass of two different branches of the AGNES tree (corresponding to two groups of sinks that are split at a given level based on phase-space distance).

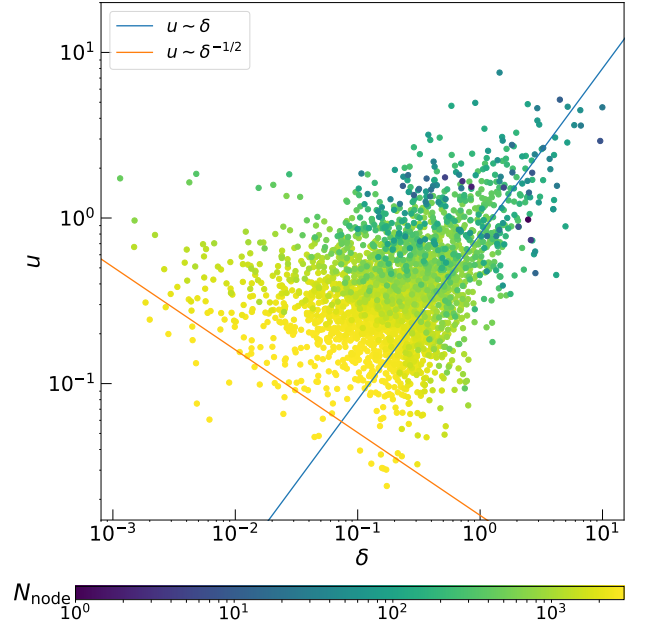


**Figure 8.** Scatter plot of the relative velocity between the centres-of-mass of two different sub-clumps corresponding to a given node in the AGNES tree as a function of their distance. The colour gradient maps the depth of the node (from the root, in blue, to the leaves, in yellow) within the AGNES tree  $N_{\text{node}}$ . The superimposed lines represent two limit slopes corresponding to rigid rotation (blue) and Keplerian motion (orange).

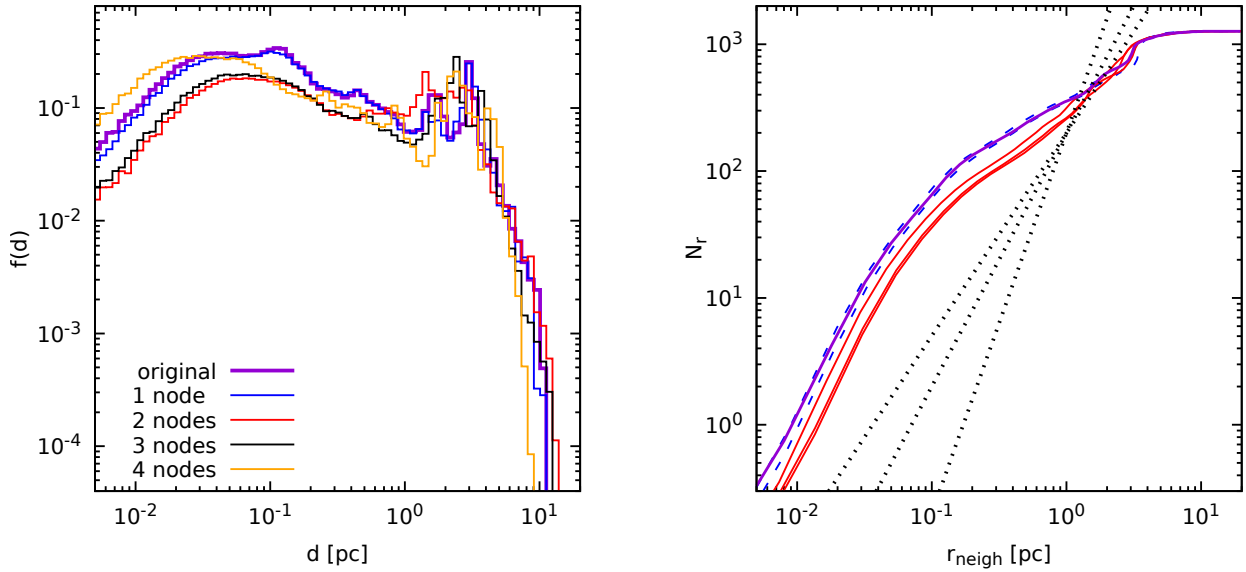


**Figure 9.** Left-hand panel: Distribution of inter-particle distances  $f(d)$  for the sink particles taken from the `m1e4` simulation (thick purple line) and 4 new generations obtained by replacing the first 1, 2, 3 and 4 nodes (corresponding to  $k = 2, 3, 4$ , and 5 in the notation used above). Right-hand panel: Average number of neighbours  $N_r$  around all particles, within a sphere with radius  $r_{\text{neigh}}$ , for different values of  $r_{\text{neigh}}$ . The thick purple line corresponds to the calculation done for the original sink particles of the `m1e4` simulation, the blue-dashed and red-solid lines represent 3 different new generations, for 1 and 2 nodes respectively. The black dotted lines represent the trend expected for distributions with a uniform fractal dimension  $\gamma = 1.6, 2$  and 3.

reference tree. This procedure may at times result in very low mass particles. We remove these planet-sized objects with a cutoff at the minimum mass of the original stars on which  $\mathcal{T}$  was learned.

In the procedure described above, the choice of the grafting depth  $k$  determines how different the new realizations are from the original system. A very low value of  $k$  produces generations that are very similar to the original one at all scales. In contrast, when  $k$  is very high, also the small scales are modified substantially. In our case, we want to generate new clusters that are similar to the original one but, at the same time, cannot be considered as its copies. We quantified how the choice of the grafting depth affects the spatial distribution of the new generations. In particular, we compared the distribution of distances and the fractality of systems generated with different values of  $k$  to that of the original cluster, for the case of `m1e4`. The left panel of Fig. 9 shows that the general shape of the distribution of inter-particle distances is well reproduced in all cases, with slight differences below the parsec scale. The peaks correspond to sub-clumps of sinks, that are formed in different numbers and sizes in each realization. Predictably, the realization obtained by modifying just one node matches the original better than those that modify two or three nodes, and the one with four modified nodes is deviating the most from the original. This suggests that very few changes ( $k = 3$ ) are sufficient to obtain generations not identical to the original one.

As a confirmation of this, in the right-hand panel of Fig. 9, we have computed the average number of neighbours of each sink within a given distance, following Ballone et al. (2020). The distribution of neighbours of `m1e4` is not described by a single power law of non integer index  $\beta$ , as one would expect in a simple fractal structure, but presents two slope changes at around  $\approx 10^{-1}$  and  $\approx 2$  pc (see also Ballone et al. 2020). To guide the eye, the three dotted lines mark the theoretical distance distributions in the case of a pure fractal distribution with  $N_r \propto r_{\text{neigh}}^{1.6}$  and the two lattice distributions in two and three dimensions with  $N_r \propto r_{\text{neigh}}^2$  and  $N_r \propto r_{\text{neigh}}^3$ , respectively. The generated realizations for  $k = 2$  and  $k = 3$  match

the general trend and the changes in the slope of the original simulation very well, showing that our method captured the underlying structure of the particle distribution in the 3D space at all scales. Like for the inter-particle distance distribution, the choice of  $k = 2$  produces only minimal differences from the original `m1e4` profile.

In the following, we will focus on generations with  $k = 3$ , which is the smallest value to produce clusters that are distinguishable from the original one.

## 4 RESULTS

### 4.1 Properties of the newly generated systems

In this Section, we discuss the properties of the systems generated using our procedure starting from the simulation `m1e4`, as this has the highest resolution (i.e. largest number of SPH particles for a given total mass).

Figure 10 shows the spatial distributions of five new generations obtained with the method described in Section 3.3 and compared to the original one. The new generations show a strong sub-structured configuration, with a different number of clumps, depending on the single realization, that has drawn branches from different simulations. Also, a strong degree of mass segregation is still present in the single sub-clumps, as highlighted by the colour coding. This primordial mass segregation in the individual realizations qualitatively matches the one present in the original cluster.

In Fig. 11, we compare the mass distribution of `m1e4` to those of the new generations. In this case, our method leaves the slope of the mass function largely unaltered for most of the mass spectrum. At the boundaries of the mass spectrum, some discrepancies are present. This is due to the fact that the change in the first nodes may split up a relatively small particle more times than in the original cluster, and leaves more massive particles less split. This explains the higher number of particles at the boundaries of the mass spectrum with respect to the original one. The sharper cut-off at  $m \approx 10^{-1} M_\odot$  is



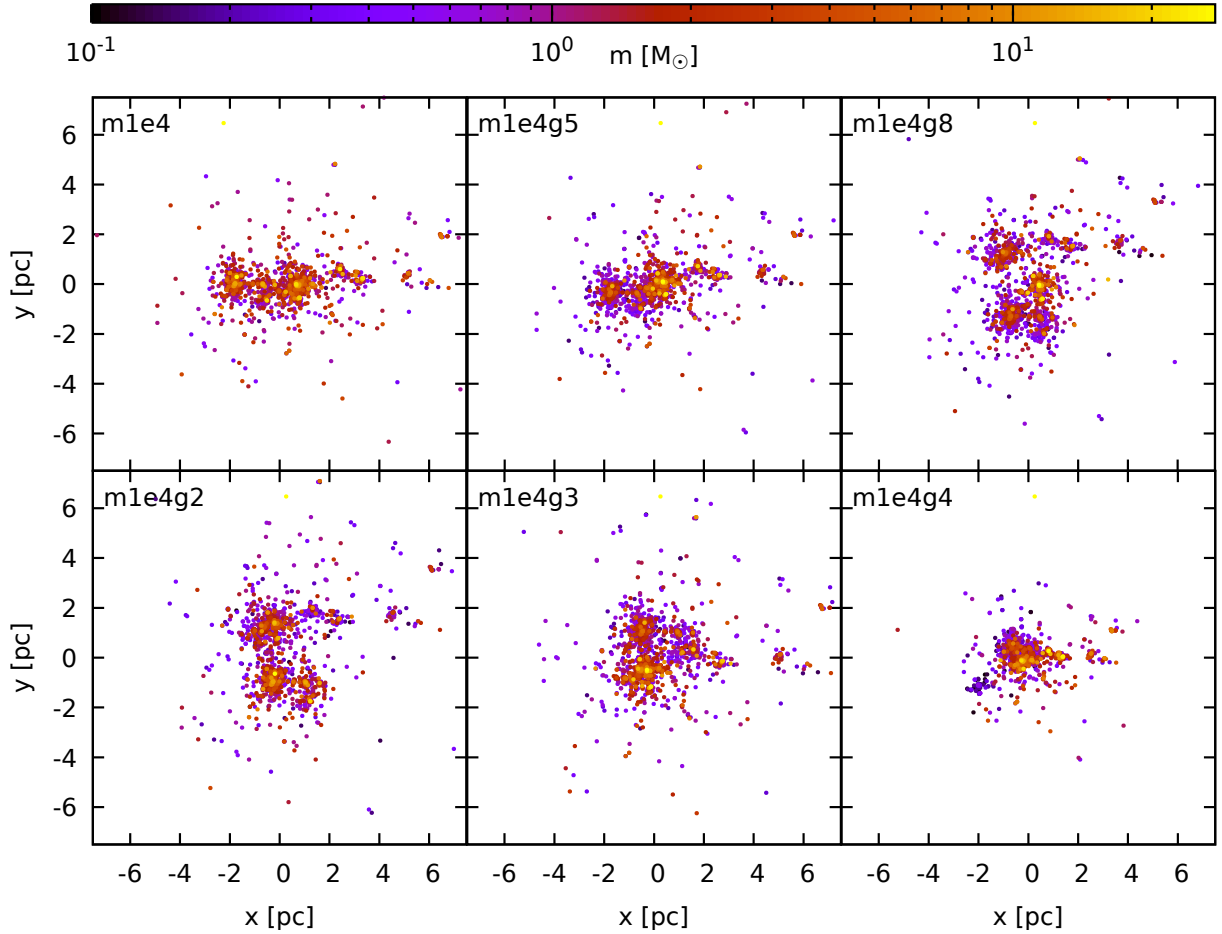


**Figure 10.**  $x - y$  projection of the m1e4 system (top left panel, see also Fig. 1) and five different AGNES generations. The colour code marks the different masses of the sink particles and their re-generations.

due to the fact that all masses below this threshold are systematically removed. In general, the fit with Eq. 2 is rather good, yielding values of  $\gamma$  around 2.3, reminiscent of a Salpeter (1955) slope.

Figure 12 shows the velocity distribution of the new generations, as compared to the original one. The distributions look similar, both on the low-velocity tail, where the Maxwell-Boltzmann trend seems to be preserved, and on the sharper power-law trend at high velocities. Due to the redistribution of particle positions and velocities and mass splitting in the generation process, the value of the total virial ratio  $\alpha_{\text{vir}}$  is significantly altered (with respect, in this case, to the value of 1.19 for the m1e4 case) ranging from a minimum of 0.46 to a maximum of 2.08. Clearly, future dynamical evolution depends heavily on the virial ratio, which, in turn, is heavily affected by the left tail of the particle pairwise distances. There is indeed a margin of variation in short distances between realizations, as shown in Fig. 9. However, the shortest distances in any stellar system essentially correspond to binary-star semi-axes. Our hydro-dynamical simulations were not designed to faithfully reproduce an observational initial mass function (Ballone et al. 2021) nor to capture binary properties. In Torniamenti et al. (2021), we introduce a realistic binary distribution with a separate procedure. While binary binding energy is a large fraction of the total binding energy in many realistic scenarios, the time scale over which this energy is exchanged with the cluster at large is much longer than the dissolution time for the typical system under consideration: hard binaries are dynamically inert in the short term. To check that this is

the source of the observed virial ratio mismatch, we have operated two diagnostics. First of all, we have recomputed the virial ratio  $\alpha_{\text{vir}}$   $N_s$  times excluding each time a different particle. This gives us a robust way to quantify the virial ratio, as the spread in the resulting distribution will be driven by instances in which a member of a very close binary was excluded. In all cases, the value of  $\alpha_{\text{vir}}$  of the original system lies well inside the distribution of  $\alpha_{\text{vir}}$  obtained by removing one particle at time from a given generation.

Secondly, we have also computed the  $\alpha_{\text{vir}}$  by excluding the binding energy of stars with separation under a varying threshold between one tenth and one half of the average inter-particle distance. We found that the large variations in the value of  $\alpha_{\text{vir}}$  observed for the generated clusters is essentially due to the different distributions of tightly bound particles in the generated clusters and the parent sink particle system produced by our SPH simulations. Thus, different values of the virial ratio will result in a similar dynamical evolution on the time scales of interest, as shown below by evolving our realization through direct  $N$ -body simulations. We list the nominal virial coefficients of our generated realizations together with other properties in Table 2.

#### 4.2 $N$ -body simulations

Our method aims to generate large samples of initial conditions for  $N$ -body simulations. To test that our realizations are indeed suit-

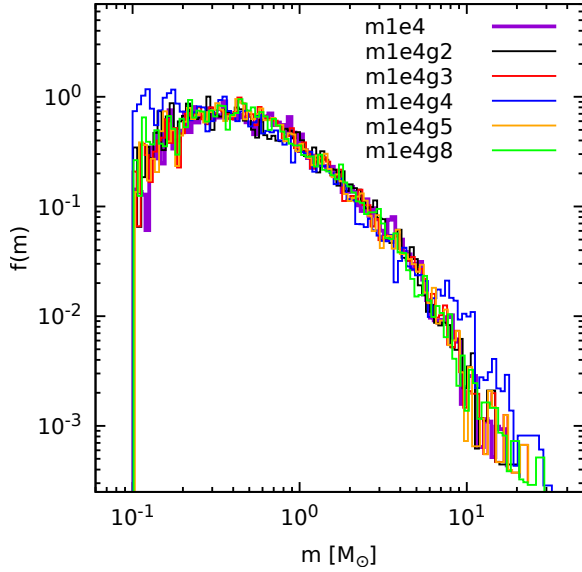


**Figure 11.** Mass spectrum of the sink particles of simulation *m1e4* (thick purple line) and of four different generated systems with four splits (thin lines).

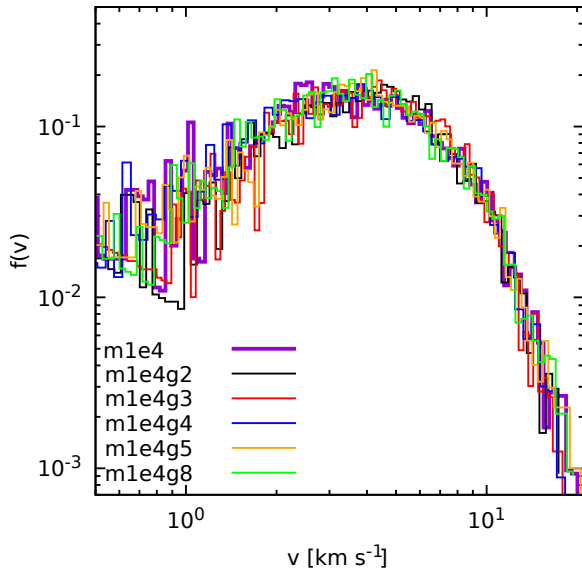


**Figure 12.** Velocity distribution for the same systems as in Fig. 11.

able for this use, we evolve via direct  $N$ -body simulations the three original clusters (*m1e4*, *m3e4* and *m6e4*) and 10 different generated clusters per each of the three original ones. Finding that the evolution of the generated clusters is neither identical nor dramatically different with respect to the original cluster is one of the main test-beds of our method. In fact, our method can be successfully used only if the new clusters evolve in a similar way as the original one, but are sufficiently different not to be an exact copy. Ideally, the generated clusters should behave as different random realizations of the same underlying physical distributions.

We ran our simulations with the direct  $N$ -body code *NBODY6++GPU* (Wang et al. 2015). Thanks to a neighbour scheme (Nitadori & Aarseth 2012), *NBODY6++GPU* efficiently handles the collisional force contributions at short time scales as well as those at longer time intervals, to which all the members in the system con-

**Table 2.** Properties of the generated clusters starting from *m1e4*, *m3e4* and *m6e4*.

Name	$N_s$	$N_c$	$\alpha_{\text{vir}}$	$\gamma$	$M_{\text{sink}} [M_\odot]$
<i>m1e4g1</i>	2006	6	0.60	2.3	$4.20 \times 10^3$
<i>m1e4g2</i>	2509	6	1.41	2.3	$4.20 \times 10^3$
<i>m1e4g3</i>	2512	6	1.57	2.3	$4.20 \times 10^3$
<i>m1e4g4</i>	1998	8	0.60	2.3	$4.20 \times 10^3$
<i>m1e4g5</i>	2512	5	1.68	2.3	$4.20 \times 10^3$
<i>m1e4g6</i>	2491	7	1.50	2.3	$4.20 \times 10^3$
<i>m1e4g7</i>	2081	8	0.48	2.3	$4.20 \times 10^3$
<i>m1e4g8</i>	2512	9	1.81	2.3	$4.20 \times 10^3$
<i>m1e4g9</i>	2196	4	0.46	2.3	$4.20 \times 10^3$
<i>m1e4g10</i>	2496	7	1.57	2.3	$4.20 \times 10^3$
<hr/>					
<i>m3e4g1</i>	2765	5	0.80	2.2	$1.03 \times 10^4$
<i>m3e4g2</i>	2805	7	1.39	2.2	$1.03 \times 10^4$
<i>m3e4g3</i>	2811	5	1.16	2.2	$1.03 \times 10^4$
<i>m3e4g4</i>	2719	5	1.20	2.2	$1.03 \times 10^4$
<i>m3e4g5</i>	2747	7	1.48	2.2	$1.03 \times 10^4$
<i>m3e4g6</i>	2774	6	1.40	2.2	$1.03 \times 10^4$
<i>m3e4g7</i>	2750	6	1.46	2.2	$1.03 \times 10^4$
<i>m3e4g8</i>	2770	7	1.13	2.2	$1.03 \times 10^4$
<i>m3e4g9</i>	2628	7	0.94	2.2	$1.03 \times 10^4$
<i>m3e4g10</i>	2764	6	0.94	2.2	$1.03 \times 10^4$
<hr/>					
<i>m6e4g1</i>	2747	7	1.65	2.1	$2.04 \times 10^4$
<i>m6e4g2</i>	2823	7	1.80	2.1	$2.04 \times 10^4$
<i>m6e4g3</i>	2900	5	1.82	2.1	$2.04 \times 10^4$
<i>m6e4g4</i>	2718	6	1.66	2.1	$2.04 \times 10^4$
<i>m6e4g5</i>	2967	6	1.75	2.1	$2.04 \times 10^4$
<i>m6e4g6</i>	2752	5	1.30	2.1	$2.04 \times 10^4$
<i>m6e4g7</i>	2998	6	1.55	2.1	$2.04 \times 10^4$
<i>m6e4g8</i>	2833	6	1.36	2.1	$2.04 \times 10^4$
<i>m6e4g9</i>	3001	6	1.82	2.1	$2.04 \times 10^4$
<i>m6e4g10</i>	3015	5	1.82	2.1	$2.04 \times 10^4$

Column 1 is the name of the generated cluster; column 2 is the number of macroscopic sub-clumps; column 3 is the virial ratio; column 4 is the  $\gamma$  coefficient of the mass-spectrum fitting function of eq. 2; column 6 is the total mass of the stars.

tribute. The force integration also includes a solar neighbourhood-like static external tidal field (Wang et al. 2016). Stellar evolution is not included in our runs, for the sake of simplicity and to make the comparison with the original cluster more straightforward. We evolved the clusters for 10 Myr.

Table 2 shows the main initial properties of the generated clusters for which we ran the  $N$ -body simulations. Figure 13 shows the projection in the  $x - y$  plane of the original *m1e4* cluster and of four generations, at different times. The global evolution of the new generated clusters shows a variety of configurations depending on the different distribution of mass. In some cases, distinct sub-clumps are present at  $t > 1$  Myr and tidally interact with each other before eventually merging. In the case of *m1e4g4*, two distinct sub-clumps are still present at 10 Myr.

A more quantitative description of the global evolution of the clusters can be given in terms of the evolution of the 10% and 50% Lagrangian radii ( $r_{10}$  and  $r_{50}$ ), centred in the centre of density<sup>4</sup>. Figures 14 and 15 show the evolution of  $r_{10}$  and  $r_{50}$  for the original clusters and the generated ones. In all the cases, the original

<sup>4</sup> The local density around each star was calculated as the density of the sphere that includes the 300 closest stars.

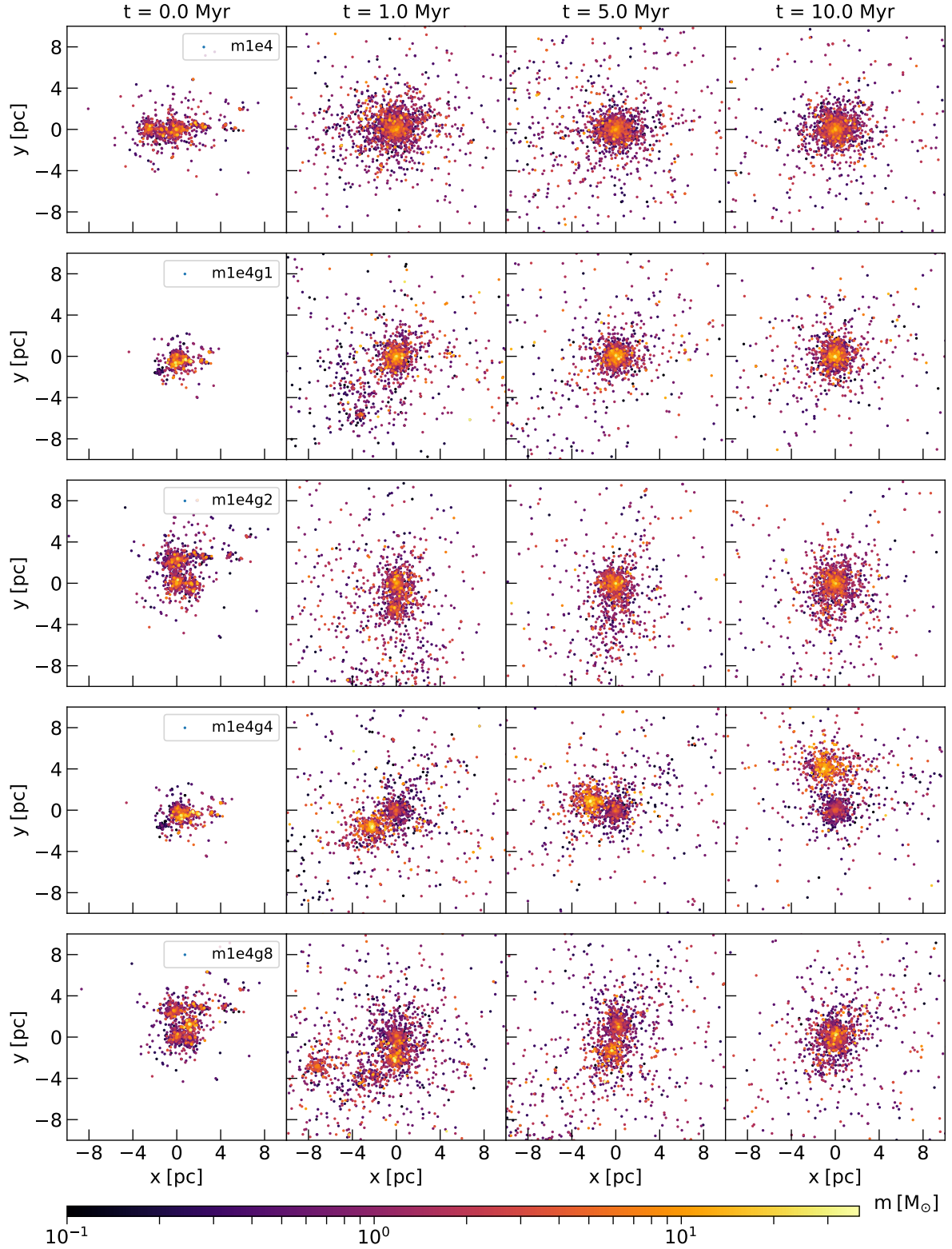


**Figure 13.** Projection in the  $x - y$  plane of the original cluster (m1e4, upper panel) and four different generated clusters (lower panels) as a function of time. The clusters are shown at their initial configuration (first column) and at three different time steps: 1 Myr (second column), 5 Myr (third column) and 10 Myr (last column). The colour code marks the different masses of the sink particles and their generations.

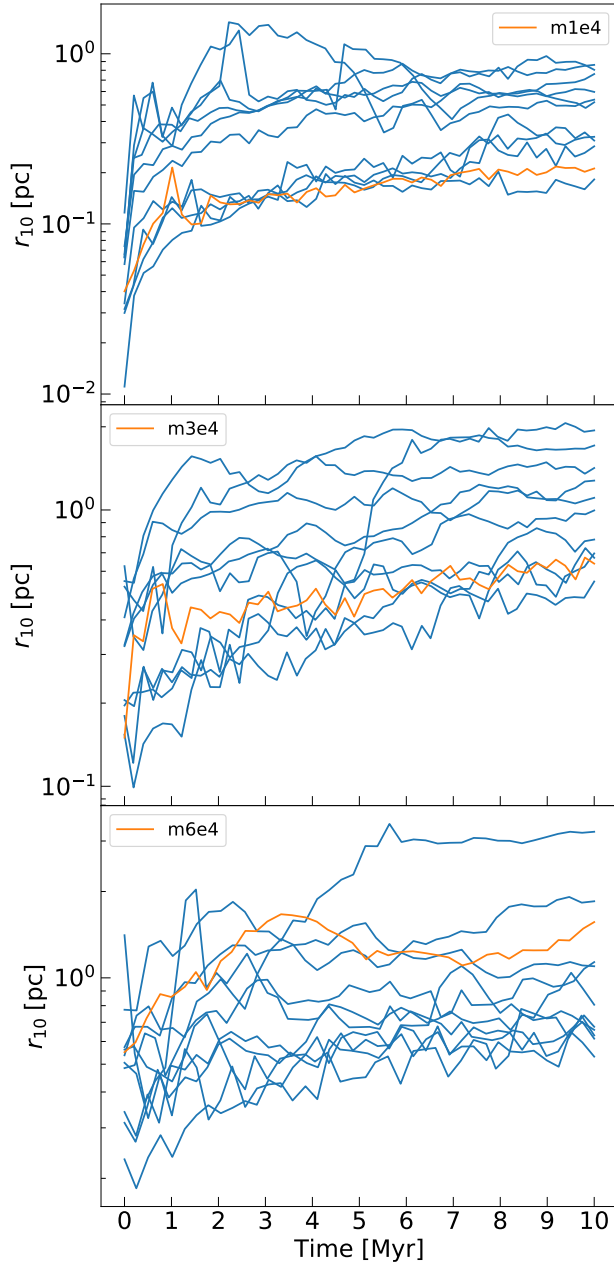


**Figure 14.** Evolution of the 10% Lagrangian radius of the original sink particles and ten different generations for **m1e4** (upper panel), **m3e4** (middle panel), and **m6e4** (lower panel). The orange line represents the original sink particle system, and the blue lines are the generated clusters.

evolution lies within the limits of the distribution of the generated clusters, that shows a large spread. This spread is consistent with the large stochastic fluctuations that we expect in the evolution of such low-mass clusters (e.g., [Torniamenti et al. 2021](#)).

## 5 DISCUSSION AND CONCLUSIONS

We introduced a new method for generating a number of new realizations from a given set of initial conditions (particle positions and velocities) produced by a hydro-dynamical simulation. The re-

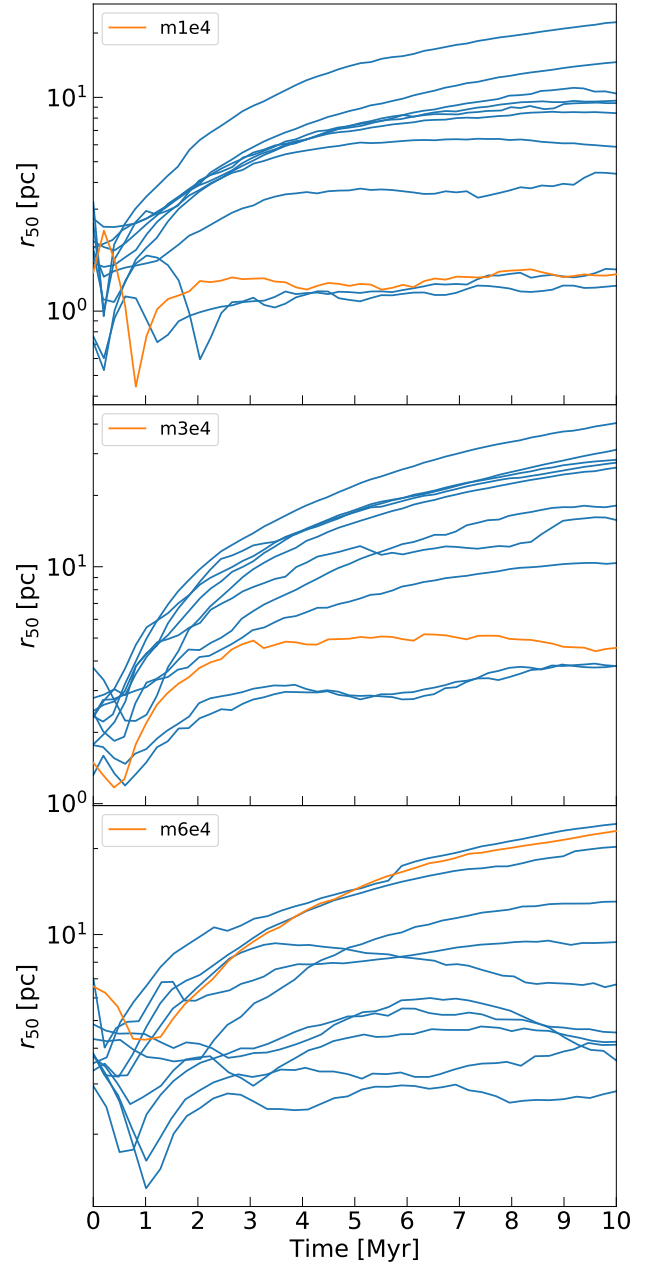


**Figure 15.** Same as Figure 14 but for the 50% Lagrangian radius.

alizations are built to display a different large scale structure, but share similar properties at smaller scales, preserving in particular the fractal dimension of the original simulation. We have shown that they can be used as initial conditions for  $N$ -body simulations, producing a comparable evolution to the original cluster. This suggests that our method is suitable for drawing the initial conditions of a large set of  $N$ -body simulations at an infinitesimal fraction of the computational cost of generating initial conditions from a hydro-dynamical simulation.

Our novel approach relies on learning a hierarchical clustering structure (represented as a tree) from the original initial condition data through agglomerative clustering. This is later turned into new realizations by modifying the initial branches of the tree (encoding

the relations between the biggest sub-clumps in the simulation). This results in realizations with different macroscopic properties from the original one (e.g., the number of big clumps and their distances), while approximately preserving the characteristics of small scale structure responsible for most of dynamical evolution (e.g., the distribution of pairwise distances between individual stars). In principle, this scheme is very flexible, allowing to choose how much of the large scale structure we control directly, by choosing the number of initial branches we modify.

The realizations we obtained with our method qualitatively resemble the original simulation when visualized in three-dimensional space. In our case the original distribution of stars was generated by hydro-dynamical simulations of embedded clusters, so our new realizations appear qualitatively indistinguishable from the output of simulations. The mass spectrum and the velocity distribution are also very similar to the original simulation. The distribution of the number of neighbours as a function of distance reveals that the fractal dimension of our realization and that of the original simulation match on different scales (both show a similar multifractal pattern).

Finally, we ran direct  $N$ -body simulations of a sample of generated initial conditions for three different original star clusters. In all the cases, the new generations show a realistic evolution on all scales, bracketing that of the original one, as shown by the trend of the 10% and 50% Lagrangian radii. Our analysis suggests that this method is a promising way to generate new mass and phase-space distributions from existing hydro-dynamical simulations, thus increasing our sample of initial conditions for  $N$ -body simulations. The speedup in computation obtained by our new method is tremendous: generating initial conditions from hydro-dynamical simulations requires weeks on state-of-the-art hardware, while our procedure takes a few minutes to train an initial tree representation and fractions of a second to generate a new realization.

## ACKNOWLEDGEMENTS

MP contribution to this material is based upon work supported by Tamkeen under the NYU Abu Dhabi Research Institute grant CAP3. MM, AB and GI acknowledge financial support from the European Research Council for the ERC Consolidator grant DEMOBLOCK, under contract no. 770017. PFDC acknowledges financial support from MIUR-PRIN2017 project *Coarse-grained description for non-equilibrium systems and transport phenomena (CO-NEST)* n.201798CZL.

## DATA AVAILABILITY

The data underlying this article will be shared on reasonable request to the corresponding authors.

## REFERENCES

Alessandrini E., Lanzoni B., Ferraro F. R., Miocchi P., Vesperini E., 2016, *ApJ*, **833**, 252  
 Allison R. J., Goodwin S. P., Parker R. J., Portegies Zwart S. F., de Grijs R., 2010, *MNRAS*, **407**, 1098  
 An J. H., Evans N. W., 2006, *AJ*, **131**, 782  
 Antoja T., et al., 2018, *Nature*, **561**, 360  
 Bahcall J. N., Ostriker J. P., 1975, *Nature*, **256**, 23  
 Ballone A., Mapelli M., Di Carlo U. N., Tornamenti S., Spera M., Rastello S., 2020, *MNRAS*, **496**, 49

Ballone A., Tornamenti S., Mapelli M., Di Carlo U. N., Spera M., Rastello S., Gaspari N., Iorio G., 2021, *MNRAS*, **501**, 2920  
 Banerjee S., Baumgardt H., Kroupa P., 2010, *MNRAS*, **402**, 371  
 Bastian N., Lardo C., 2015, *MNRAS*, **453**, 357  
 Bastian N., Lardo C., 2018, *ARA&A*, **56**, 83  
 Bastian N., Gieles M., Ercolano B., Gutermuth R., 2009, *MNRAS*, **392**, 868  
 Bate M. R., 2009, *MNRAS*, **392**, 1363  
 Bate M. R., Bonnell I. A., Price N. M., 1995, *MNRAS*, **277**, 362  
 Baumgardt H., Makino J., Ebisuzaki T., 2004, *ApJ*, **613**, 1143  
 Baumgardt H., Makino J., Hut P., 2005, *ApJ*, **620**, 238  
 Beaumont D., Stepney S., 2009, in 2009 IEEE Congress on Evolutionary Computation. pp 2446–2453  
 Beccari G., Pasquato M., De Marchi G., Dalessandro E., Trenti M., Gill M., 2010, *ApJ*, **713**, 194  
 Bertin G., Stiavelli M., 1984, *A&A*, **137**, 26  
 Bianchini P., Varri A. L., Bertin G., Zocchi A., 2013, *ApJ*, **772**, 67  
 Boekholt T., Portegies Zwart S., 2015, *Computational Astrophysics and Cosmology*, **2**, 2  
 Boley A. C., 2009, *ApJ*, **695**, L53  
 Boley A. C., Hayfield T., Mayer L., Durisen R. H., 2010, *Icarus*, **207**, 509  
 Bonnell I. A., Bate M. R., Vine S. G., 2003, *MNRAS*, **343**, 413  
 Breen P. G., Heggie D. C., 2013, *MNRAS*, **432**, 2779  
 Burgers J. M., 1948, *Advances in Applied Mechanics*, **1**, 171  
 Cantat-Gaudin T., 2015, PhD thesis, Universita Degli Studi di Padova  
 Cantat-Gaudin T., et al., 2020, *A&A*, **640**, A1  
 Carretta E., et al., 2009, *A&A*, **505**, 117  
 Chardin J., Bianchini P., 2021, *MNRAS*,  
 Chomsky N., 1959, *Information and Control*, **2**, 137  
 Chung C., Pasquato M., Lee S.-Y., di Carlo U. N., An D., Yoon S.-J., Lee Y.-W., 2019, *ApJ*, **883**, L31  
 Clayton I., Gieles M., Varri A. L., Heggie D. C., Zocchi A., 2019, *MNRAS*, **487**, 147  
 Corsaro E., et al., 2017, *Nature Astronomy*, **1**, 0064  
 D'Alessio P., Calvet N., Hartmann L., 2001, *ApJ*, **553**, 321  
 D'Antona F., Caloi V., 2004, *ApJ*, **611**, 871  
 D'Antona F., Ventura P., 2007, *MNRAS*, **379**, 1431  
 D'Antona F., Caloi V., Montalbán J., Ventura P., Gratton R., 2002, *A&A*, **395**, 69  
 D'Antona F., Vesperini E., D'Ercole A., Ventura P., Milone A. P., Marino A. F., Tailo M., 2016, *MNRAS*, **458**, 2122  
 D'Ercole A., Vesperini E., D'Antona F., McMillan S. L. W., Recchi S., 2008, *MNRAS*, **391**, 825  
 D'Ercole A., D'Antona F., Ventura P., Vesperini E., McMillan S. L. W., 2010, *MNRAS*, **407**, 854  
 Dale J. E., Ercolano B., Bonnell I. A., 2015, *MNRAS*, **451**, 987  
 Dalessandro E., Raso S., Kamann S., Bellazzini M., Vesperini E., Bellini A., Beccari G., 2021, arXiv e-prints, p. arXiv:2105.02246  
 Daniel K. J., Heggie D. C., Varri A. L., 2017, *MNRAS*, **468**, 1453  
 Davies M. B., Hansen B. M. S., 1998, *MNRAS*, **301**, 15  
 Davies M., Efsthathiou G., Frenk C. S., White S. D. M., 1985, *ApJ*, **292**, 371  
 Decressin T., Meynet G., Charbonnel C., Prantzos N., Ekström S., 2007, *A&A*, **464**, 1029  
 Di Carlo U. N., Giacobbo N., Mapelli M., Pasquato M., Spera M., Wang L., Haardt F., 2019, *MNRAS*, **487**, 2947  
 Di Cintio P., Casetti L., 2019, *MNRAS*, **489**, 5876  
 Di Cintio P., Casetti L., 2020, in Bragaglia A., Davies M., Sills A., Vesperini E., eds, Vol. 351, Star Clusters: From the Milky Way to the Early Universe, pp 426–429 (arXiv:1907.12774), doi:10.1017/S1743921319006744  
 Dib S., Henning T., 2019, *A&A*, **629**, A135  
 Dinnbier F., Kroupa P., 2020, *A&A*, **640**, A84  
 Djorgovski S., 1995, *ApJ*, **438**, L29  
 Drukier G. A., 1996, *MNRAS*, **280**, 498  
 Eddy S. R., 2004, *Nature biotechnology*, **22**, 1315  
 Fabricius M. H., et al., 2014, *ApJ*, **787**, L26  
 Federrath C., Klessen R. S., 2012, *ApJ*, **761**, 156  
 Feng Y., Modi C., 2017, *Astronomy and Computing*, **20**, 44  
 Ferraro F. R., et al., 2018, *ApJ*, **860**, 50



- Fujii M. S., Portegies Zwart S., 2016, *ApJ*, **817**, 4
- Gaia Collaboration et al., 2018, *A&A*, **616**, A12
- Gavagnin E., Bleuler A., Rosdahl J., Teyssier R., 2017, *MNRAS*, **472**, 4155
- Geen S., Hennebelle P., Tremblin P., Rosdahl J., 2016, *MNRAS*, **463**, 3129
- Gieles M., Zocchi A., 2015, *MNRAS*, **454**, 576
- Goodfellow I. J., Pouget-Abadie J., Mirza M., Xu B., Warde-Farley D., Ozair S., Courville A., Bengio Y., 2014, arXiv e-prints, p. [arXiv:1406.2661](https://arxiv.org/abs/1406.2661)
- Goodman J., Heggie D. C., Hut P., 1993, *ApJ*, **415**, 715
- Goodwin S. P., Whitworth A. P., 2004, *A&A*, **413**, 929
- Gratton R., Sneden C., Carretta E., 2004, *ARA&A*, **42**, 385
- Gratton R. G., Carretta E., Bragaglia A., 2012, *A&ARv*, **20**, 50
- Gratton R., Bragaglia A., Carretta E., D'Orazi V., Lucatello S., Sollima A., 2019, *A&ARv*, **27**, 8
- Hemsendorf M., Merritt D., 2002, *ApJ*, **580**, 606
- Jebara T., 2012, Machine learning: discriminative and generative. The Springer International Series in Engineering and Computer Science Vol. 755, Springer Science & Business Media
- Jelinek F., Lafferty J. D., Mercer R. L., 1992, in Laface P., De Mori R., eds, Speech Recognition and Understanding. Springer Berlin Heidelberg, Berlin, Heidelberg, pp 345–360
- Kamann S., et al., 2018, *MNRAS*, **473**, 5591
- Kandrup H. E., Sideris I. V., 2003, *ApJ*, **585**, 244
- Kaufman L., Rousseeuw P. J., 1990, Finding groups in data. an introduction to cluster analysis. Wiley Series in Probability and Statistics
- King I. R., 1966, *AJ*, **71**, 64
- Klessen R. S., Burkert A., 2000, *ApJS*, **128**, 287
- Krause M., Charbonnel C., Decressin T., Meynet G., Prantzos N., 2013, *A&A*, **552**, A121
- Krumholz M. R., Klein R. I., McKee C. F., 2012, *ApJ*, **754**, 71
- Kuepper A. H. W., Maschberger T., Kroupa P., Baumgardt H., 2011, *McLuster: A Tool to Make a Star Cluster* (ascl:1107.015)
- Kulkarni S. R., Hut P., McMillan S., 1993, *Nature*, **364**, 421
- Küpper A. H. W., Maschberger T., Kroupa P., Baumgardt H., 2011, *MNRAS*, **417**, 2300
- Lada C. J., Lada E. A., 2003, *ARA&A*, **41**, 57
- Lee Y.-N., Hennebelle P., 2016, *A&A*, **591**, A30
- Lee Y.-N., Hennebelle P., 2019, *A&A*, **622**, A125
- Lee Y.-W., Demarque P., Zinn R., 1994, *ApJ*, **423**, 248
- Lee Y. W., Joo J. M., Sohn Y. J., Rey S. C., Lee H. C., Walker A. R., 1999, *Nature*, **402**, 55
- Lee Y.-W., et al., 2005, *ApJ*, **621**, L57
- Leigh N. W. C., Lützgendorf N., Geller A. M., Maccarone T. J., Heinke C., Sesana A., 2014, *MNRAS*, **444**, 29
- Li H., Vogelsberger M., Marinacci F., Gnedin O. Y., 2019, *MNRAS*, **487**, 364
- Lindenmayer A., 1968a, *Journal of Theoretical Biology*, **18**, 280
- Lindenmayer A., 1968b, *Journal of Theoretical Biology*, **18**, 300
- Lupton R. H., Gunn J. E., 1987, *AJ*, **93**, 1106
- Lynden-Bell D., 1962, *MNRAS*, **123**, 447
- Manwadkar V., Trani A. A., Leigh N. W. C., 2020, *MNRAS*, **497**, 3694
- Mapelli M., 2016, *MNRAS*, **459**, 3432
- Mapelli M., 2017, *MNRAS*, **467**, 3255
- Marino A. F., Villanova S., Piotto G., Milone A. P., Momany Y., Bedin L. R., Medling A. M., 2008, *A&A*, **490**, 625
- Michie R. W., Bodenheimer P. H., 1963, *MNRAS*, **126**, 269
- Milone A. P., Bedin L. R., Piotto G., Anderson J., 2009, *A&A*, **497**, 755
- Murphy D. N. A., Geach J. E., Bower R. G., 2012, *MNRAS*, **420**, 1861
- Nitadori K., Aarseth S. J., 2012, *MNRAS*, **424**, 545
- Pang X., Shen S., Shao Z., 2018, *ApJ*, **868**, L9
- Pang X., Li Y., Tang S.-Y., Pasquato M., Kouwenhoven M. B. N., 2020, arXiv e-prints, p. [arXiv:2008.02803](https://arxiv.org/abs/2008.02803)
- Park S.-M., Goodwin S. P., Kim S. S., 2018, *MNRAS*, **478**, 183
- Parker R. J., Goodwin S. P., Allison R. J., 2011, *MNRAS*, **418**, 2565
- Parker R. J., Wright N. J., Goodwin S. P., Meyer M. R., 2014, *MNRAS*, **438**, 620
- Pasquato M., Bertin G., 2008, *A&A*, **489**, 1079
- Pasquato M., Bertin G., 2010, *A&A*, **512**, A35
- Pasquato M., Masiuk N., 2019, *Research Notes of the American Astronomical Society*, **3**, 179
- Pasquato M., Milone A., 2019, arXiv e-prints, p. [arXiv:1906.04983](https://arxiv.org/abs/1906.04983)
- Pasquato M., Trenti M., De Marchi G., Gill M., Hamilton D. P., Miller M. C., Stiavelli M., van der Marel R. P., 2009, *ApJ*, **699**, 1511
- Pasquato M., Raimondo G., Brocato E., Chung C., Moraghan A., Lee Y. W., 2013, *A&A*, **554**, A129
- Pasquato M., de Luca A., Raimondo G., Carini R., Moraghan A., Chung C., Brocato E., Lee Y.-W., 2014, *ApJ*, **789**, 28
- Pasquato M., Mocchi P., Won S. B., Lee Y.-W., 2016, *ApJ*, **823**, 135
- Pedregosa F., et al., 2011, *Journal of Machine Learning Research*, **12**, 2825
- Piotto G., et al., 2015, *AJ*, **149**, 91
- Plummer H. C., 1911, *MNRAS*, **71**, 460
- Portegies Zwart S. F., Baumgardt H., Hut P., Makino J., McMillan S. L. W., 2004, *Nature*, **428**, 724
- Prendergast K. H., Tomer E., 1970, *AJ*, **75**, 674
- Prusinkiewicz P., Hanan J., 2013, Lindenmayer systems, fractals, and plants. Lecture notes in Biomathematics Vol. 79, Springer Science & Business Media
- Rabiner L., Juang B., 1986, *IEEE ASSP Magazine*, **3**, 4
- Reina-Campos M., Kruijssen J. M. D., Pfeffer J. L., Bastian N., Crain R. A., 2019, *MNRAS*, **486**, 5838
- Ruthotto L., Haber E., 2021, arXiv e-prints, p. [arXiv:2103.05180](https://arxiv.org/abs/2103.05180)
- Safonova M., Shastri P., 2010, *Ap&SS*, **325**, 47
- Salpeter E. E., 1955, *ApJ*, **121**, 161
- Seifried D., et al., 2017, *MNRAS*, **472**, 4797
- Tailo M., et al., 2015, *Nature*, **523**, 318
- Tailo M., et al., 2020, *MNRAS*, **498**, 5745
- Torniamenti S., Ballone A., Mapelli M., Gaspari N., Di Carlo U. N., Rastello S., Giacobbo N., Pasquato M., 2021, arXiv e-prints, p. [arXiv:2104.12781](https://arxiv.org/abs/2104.12781)
- Trenti M., Bertin G., 2005, *A&A*, **429**, 161
- Umbreit S., Rasio F. A., 2013, *ApJ*, **768**, 26
- Varri A. L., Bertin G., 2012, *A&A*, **540**, A94
- Vázquez-Semadeni E., Colín P., Gómez G. C., Ballesteros-Paredes J., Watson A. W., 2010, *ApJ*, **715**, 1302
- Ventura P., D'Antona F., 2009, *A&A*, **499**, 835
- Vesperini E., McMillan S. L. W., D'Ercole A., D'Antona F., 2010, *ApJ*, **713**, L41
- Wadsley J. W., Stadel J., Quinn T., 2004, *New Astron.*, **9**, 137
- Wadsley J. W., Keller B. W., Quinn T. R., 2017, *MNRAS*, **471**, 2357
- Wall J. E., McMillan S. L. W., Mac Low M.-M., Klessen R. S., Portegies Zwart S., 2019, *ApJ*, **887**, 62
- Wang L., Hernandez D. M., 2021, arXiv e-prints, p. [arXiv:2104.10843](https://arxiv.org/abs/2104.10843)
- Wang L., Spurzem R., Aarseth S., Nitadori K., Berczik P., Kouwenhoven M. B. N., Naab T., 2015, *MNRAS*, **450**, 4070
- Wang L., et al., 2016, *MNRAS*, **458**, 1450
- Ward J. H., 1963, *Journal of the American statistical association*, **58**, 236
- Ward J. L., Kruijssen J. M. D., Rix H.-W., 2020, *MNRAS*, **495**, 663
- Wilson C. P., 1975, *AJ*, **80**, 175
- Zamora-Avilés M., et al., 2019, *MNRAS*, **487**, 2200
- Zaritsky D., Zabludoff A. I., Gonzalez A. H., 2011, *ApJ*, **727**, 116
- de Vita R., Trenti M., Bianchini P., Askar A., Giersz M., van de Ven G., 2017, *MNRAS*, **467**, 4057

This paper has been typeset from a  $\text{\LaTeX}$  file prepared by the author.